lubricants

MDPI

Article

Static and Dynamic Performances of Novel Aerostatic Bearings with Primary and Secondary Orifice Restrictors

Puliang Yu [1,2,3,*], Te Zuo [1,2,3], Jiong Lu [1,2,3], Min Zhong [1,2,3] and Liping Zhang [1,2,3,*]

[1] The State Key Laboratory of Refractories and Metallurgy, Wuhan University of Science and Technology, Wuhan 430081, China; zt11655@wust.edu.cn (T.Z.); 202203703072@wust.edu.cn (J.L.); zhongmin@wust.edu.cn (M.Z.)
[2] Key Laboratory of Metallurgical Equipment and Control Technology of Ministry of Education, Wuhan University of Science and Technology, Wuhan 430081, China
[3] Hubei Key Laboratory of Mechanical Transmission and Manufacturing Engineering, Wuhan University of Science and Technology, Wuhan 430081, China
* Correspondence: polo2008@wust.edu.cn (P.Y.); zhangliping@wust.edu.cn (L.Z.)

Abstract: Aerostatic bearings are crucial support components in ultra−precision manufacturing equipment. However, improvements in the load−carrying capability (LCC) of aerostatic bearings often lead to higher intensity nano−vibrations. This paper introduces a novel primary and secondary orifice restrictor (PSOR) designed to simultaneously enhance the LCC and mitigate nano−vibrations in aerostatic bearings. The static performance of complex turbulent flows occurring within the chamber of aerostatic bearings with PSORs was investigated. The dynamic performance of the turbulent flows was analyzed through 3D transient numerical simulation using the large eddy simulation method. The LCC and nano−vibration acceleration were measured experimentally, and the results indicated that the design of the secondary orifice diameter could enhance LCC and mitigate nano−vibrations, consistent with theoretical predictions. The accuracy of the proposed model was validated, confirming the effectiveness of PSOR. In the experiments, an aerostatic bearing with a secondary orifice diameter of 0.1 mm exhibited the lowest LCC and largest nano−vibration. Conversely, an aerostatic bearing with a secondary orifice diameter of 0.26 mm exhibited the highest LCC and weakest nano−vibration. This study provides insights into the formation mechanism of turbulent vortex and interaction mechanism among the primary orifice and secondary orifices in aerostatic bearings with a PSOR.

Keywords: primary and secondary orifices restrictor; stiffness; turbulent vortex; nano−vibration

Citation: Yu, P.; Zuo, T.; Lu, J.; Zhong, M.; Zhang, L. Static and Dynamic Performances of Novel Aerostatic Bearings with Primary and Secondary Orifice Restrictors. *Lubricants* **2023**, *11*, 518. https://doi.org/10.3390/lubricants11120518

Received: 31 October 2023
Revised: 2 December 2023
Accepted: 6 December 2023
Published: 8 December 2023

1. Introduction

Aerostatic bearings are extensively used in high−precision machining and ultra−precision machining owing to their remarkable attributes, including near−zero friction, high speed, and exceptional accuracy [1–4]. However, designing nano−positioning devices with high positional accuracy is challenging because of inherent nano−vibrations induced by turbulent vortices [5–7]. Operational conditions and structural parameters, such as film thickness, supply pressure, and restrictor dimensions, influence the dynamic behavior of aerostatic bearings. Therefore, several studies have focused on optimizing restrictor designs to mitigate nano−vibrations in aerostatic bearings.

Numerous researchers have investigated the characteristics of aerostatic bearings equipped with various types of restrictors, encompassing orifice, porous, and slot configurations [8–10]. Among these, the restrictors employing orifice−type designs with a chamber are the most extensively use in aerostatic bearings. Studies have primarily focused on attributes such as load−carrying capacity (LCC), stiffness, and pressure distribution [11–13]. Boffey et al. [14,15] examined the impact of recess restrictors on static performance, and Chen et al. [16] proposed a reliable mathematical model to calculate the stiffness of journal

bearings with different restrictor designs and validated it through experiments. Chen and He [17] performed numerical simulations of the dynamic performance of aerostatic thrust bearings with various recess shapes using computational fluid dynamics (CFD) software Fluent, revealing that the LCC of aerostatic bearings with a rectangular recess is the highest. Li et al. [18] comprehensively analyzed the effects of pocketed orifice−type restrictors on aerostatic bearing performance using CFD software Fluent and through experiments, focusing on their relationships with restrictor structural parameters. However, while the chamber in the orifice−type aerostatic bearing enhances static performance, it simultaneously exacerbates pressure fluctuations and self−excited vibrations, thereby limiting motion positioning accuracy. Therefore, numerous studies have examined the complexities of pressure fluctuations and turbulent vortices near outward orifices [19,20]. Fourka et al. [21] established a non−linear model based on the finite element method to analyze the stability of air thrust bearings, revealing that the linear analysis underestimates the stability threshold compared with their non−linear model. Kawai et al. [22] experimentally demonstrated that nano−vibrations of aerostatic bearings may be attributed to air turbulence. Yoshimura et al. [23] investigated the behaviors of aerostatic bearings featuring T−shaped grooves through CFD analysis and experiments, revealing a direct correlation between nano−vibrations and pressure fluctuations stemming from transient airflow patterns along the bearing edge. Chen et al. [24] solved the full Navier–Stokes equations for the steady compressible flows to investigate turbulent vortices in the chamber using CFD software Fluent. The results from both the computational and experimental results demonstrated a direct correlation between the vibration energy of the aerostatic bearing and the intensity of the turbulent vortex. Eleshaky [25] employed the CFD method to investigate the pressure depression phenomenon in aerostatic thrust bearings. Otsu et al. [26] explored the instability of aerostatic journal bearings equipped with compound restrictors through numerical simulations and experiments. Wang et al. [27] precisely evaluated the pressure fluctuation characteristics in pneumatic hammer through the empirical mode method and experiments. Their findings indicated that vortex phenomena near the orifice restrictor outlet can induce instability in aerostatic bearings, highlighting the correlation between instability and both turbulent vortices in the chamber and the restrictor's structural parameters.

To prevent vortex generation and alleviate nano−vibrations, numerous scholars have comprehensively investigated the dynamic behaviors of aerostatic bearings, employing a combination of experimental and theoretical approaches. Aoyama et al. [28] investigated airflow characteristics and the mechanism of nano−vibrations in guideways equipped with aerostatic bearings through numerical and experimental methods. Ma et al. [29] employed the fourth−order Runge–Kutta method and finite element method to evaluate the dynamic performances of aerostatic thrust bearings with an array of damping orifices, which can effectively improve the stability of pneumatic hammers. Zhu et al. [30] explored pressure fluctuations and vortex shedding through the large eddy simulation (LES) method, demonstrating connections between pressure fluctuations and nano−vibrations in aerostatic bearings through simulations and experiments. Li et al. [31] revealed the mechanism of vortex generation using the CFD software Fluent, demonstrating the advantages of design optimization via simulation and experiment. Chen et al. [32] employed the LES method to investigate the transient flow characteristics of aerostatic bearings with an arrayed micro−orifice restrictor designed to inhibit vortex generation and mitigate nano−vibrations. Feng et al. [33] proposed 3−D printed orifice restrictors and analyzed their airflow characteristics within the recess by using the CFD software Fluent, demonstrating that aerostatic bearings with arc−orifice structures exhibited the smallest vortices in the recess by simulation and experiment. Yu et al. [34] employed the LES method to investigate the influence of a square micro−hole−arrayed restrictor on the dynamic behavior of these bearings. Both numerical simulation and experimental results indicated that the nano−vibrations of aerostatic thrust bearings can be effectively suppressed.

In summary, vortex formation must be addressed when designing orifice−type aerostatic bearings with chambers to effectively minimize nano−vibrations. In this study,

considering the mechanism of vortex formation, we developed a novel multiple−orifice restrictor known as the primary and secondary orifices restrictor (PSOR), aimed at inhibiting turbulent vortex formation and enhancing both static and dynamic performance. Dynamic characteristics were examined through the LES method, and static and dynamic behaviors, including LCC and vibration acceleration were assessed using two experimental setups. Theoretical predictions were validated by comparing the experimental results with our theoretical results. This study offers a novel approach for enhancing LCC, suppressing vortex formation, and enhancing the stability of aerostatic bearings through the optimized design of the PSOR.

2. Aerostatic Bearings with Primary and Secondary Orifice Restrictors

Figure 1 illustrates the schematic diagram and operational principle of a single−orifice−type aerostatic bearing featuring a chamber. High−pressure air enters the chamber through the single−orifice restrictor (SOR), diffuses inside, and is subsequently released into the external atmosphere. Figure 2 depicts the pressure distribution and vorticity along the symmetry plane. Notably, turbulent vortices predominantly occur near the orifice outlet. Additionally, as the orifice diameter (i.e., the orifice area) decreases, the pressure distribution and vorticity within the chamber also gradually decrease. Therefore, varying the orifice diameter can modulate pressure distribution, influencing overall stability. Consequently, the orifice diameter, or the area through which air flows, notably impacts pressure distribution and the generation of turbulent vortices within the chamber.

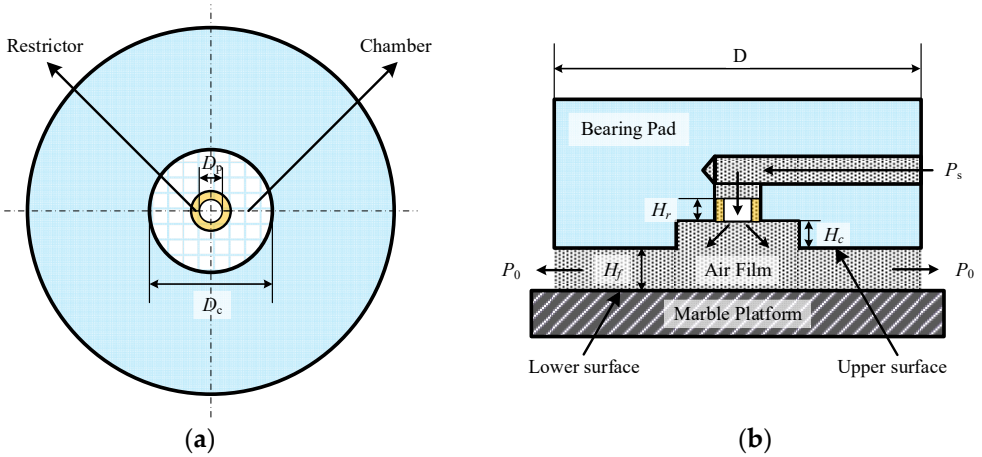

Figure 1. Structure diagram and the operational principle of aerostatic bearing with a single chamber: (**a**) bottom view; (**b**) cross−section view.

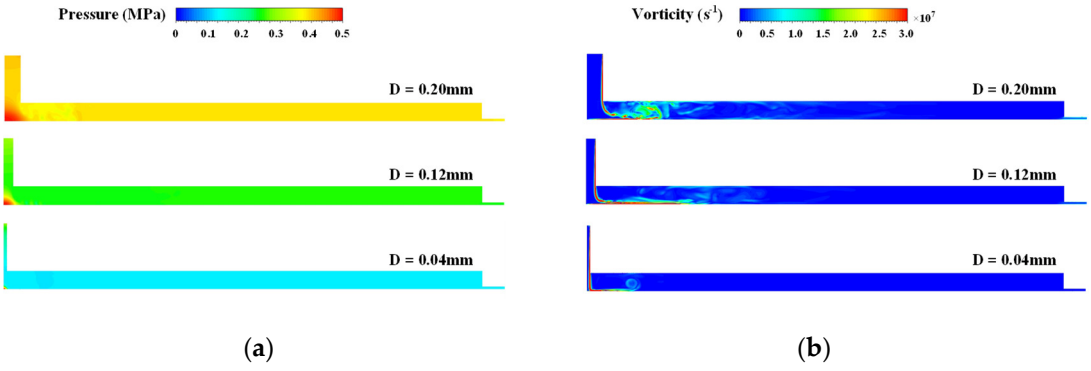

Figure 2. Cloud diagram of airflow field along the symmetrical plane: (**a**) pressure; (**b**) vorticity.

Building on the aforementioned analysis, we introduce a novel aerostatic bearing with the primary and secondary orifice restrictor (PSOR), as depicted in Figure 3. The

PSOR comprises one primary orifice and four secondary orifices. The four secondary orifices are symmetrically arranged circumferentially to ensure an even distribution of pressure in the chamber, preventing any imbalances in its gravitational center, as detailed in Table 1. The four secondary orifices facilitate the diffusion of the high−pressure gas into the chamber, resulting in a higher LCC of the aerostatic bearing. However, structural modifications to this novel type of aerostatic bearing complicate the lubrication mechanism, given the interplay and interdependence between adjacent orifices. Furthermore, the coupling effect between LCC and stability of aerostatic bearings is enhanced, necessitating a comprehensive investigation to ensure improvements in both LCC and stability.

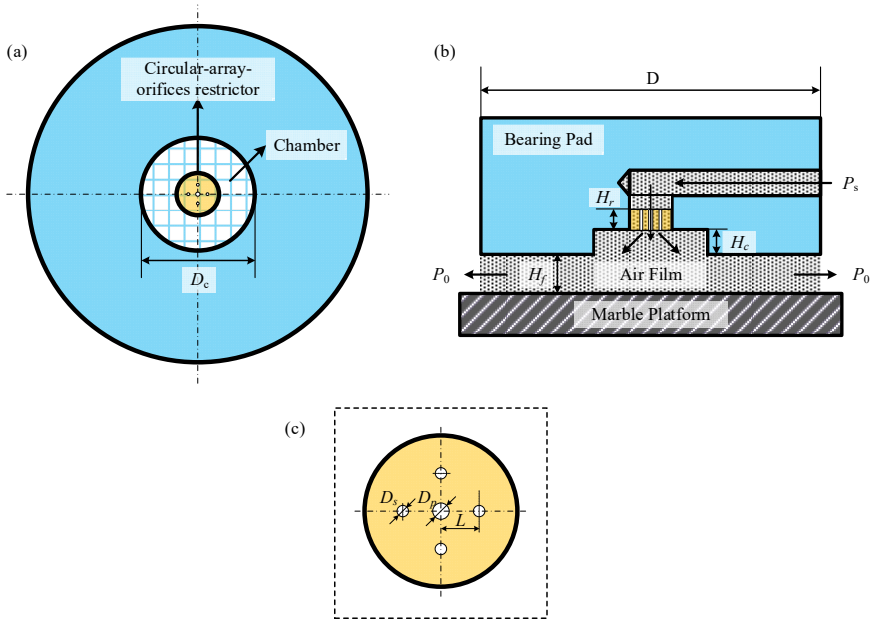

Figure 3. Schematic diagram of the aerostatic bearings with a PSOR: (**a**) bottom view of aerostatic bearing; (**b**) cross−section view of aerostatic bearing; (**c**) bottom view of PSOR.

Table 1. Structural parameters of aerostatic bearings with PSORs.

Type	Restrictor	Primary Orifice Diameter D_p (mm)	Secondary Orifice Diameter D_s (mm)	Spacing L (mm)	Chamber Height H_c (mm)	Chamber Diameter D_c (mm)	Bearing Diameter D (mm)	Orifice Height H_r (mm)
A	1 Po + 4 So	0.3	0.10~0.26	0.5	0.1	5	80	0.3
B	1 Po	0.3	0	0	0.1	5	80	0.3

3. Numerical Calculation Method

3.1. Large Eddy Simulation

The complex transient flow field characteristics of aerostatic bearings can be expressed using the Navier–Stokes equations. Li et al. [35] introduced a novel hyperbolic Navier–Stokes system (HNS) and a reconstructed discontinuous Galerkin (rDG) method for both steady and unsteady compressible viscous flows. As revealed by numerical simulations, the HNS + rDG approach is an attractive and viable alternative for solving the compressible Navier–Stokes equations. Kabir et al. demonstrated that the Reynolds Averaged Navier–Stokes (RANS) simulation method is suitable for investigating turbulence, but it may not be effective in accurately assessing the instantaneous complexities of turbulence [32]. In theory, direct numerical simulation (DNS) can precisely resolve the entire range of spatial and temporal scales of turbulence based on the Navier–Stokes equations without the need for any turbulence model. However, its computational scale is massive [30]. LESs can be

used to perform a direct numerical simulation of vortices above the grid resolution scale in a flow field, encompassing the direct computation of large−scale turbulent vortices and the simulation of small−scale turbulent vortices. The accuracy and computational scale of LESs are between those of RANS and DNS, supporting its extensive use in the complex turbulence simulation of aerostatic bearings [30,36].

We applied filtering to the time−dependent Navier–Stokes equations using the governing equations. The filtering of the continuity and momentum equations [31,36] can be defined as follows:

$$\frac{\partial \overline{\rho}}{\partial t} + \frac{\partial (\overline{\rho} \widetilde{u}_i)}{\partial x_i} = 0 \tag{1}$$

$$\frac{\partial (\overline{\rho} \widetilde{u}_i)}{\partial t} + \frac{\partial \left(\overline{\rho} \widetilde{u}_i \widetilde{u}_j\right)}{\partial x_j} = \frac{\partial \widetilde{\sigma}_{ij}}{\partial x_j} - \frac{\partial \overline{p}}{\partial x_i} - \frac{\partial \widetilde{\tau}_{ij}}{\partial x_j} \tag{2}$$

The density−weighted filter is employed as the Favre filter, where the density ρ and pressure p are spatially filtered (denoted by "−"), while the velocity u_i and u_j are density−weighted (denoted by "~"). τ_{ij} represents subgrid−scale (SGS) stress, which is modeled using an SGS model; $\widetilde{\sigma}_{ij}$ representing the viscous stress tensor resulting from molecular viscosity is denoted as follows:

$$\widetilde{\sigma}_{ij} = \mu \left(\frac{\partial \widetilde{u}_i}{\partial x_j} + \frac{\partial \widetilde{u}_j}{\partial x_i} \right) - \frac{2}{3} \mu \delta_{ij} \frac{\partial \widetilde{u}_k}{\partial x_k} \tag{3}$$

The compressible form of the subgrid−scale stress tensor is expressed as follows:

$$\widetilde{\tau}_{ij} = \overline{\rho} \widetilde{u_i u_j} - \overline{\rho} \widetilde{u}_i \widetilde{u}_j \tag{4}$$

where

$$\overline{p} = \overline{\rho} R \widetilde{T} \tag{5}$$

Filtering the energy equation can be defined as follows:

$$\frac{\partial \overline{\rho} \widetilde{h}_s}{\partial t} + \frac{\partial \overline{\rho} \widetilde{u}_i \widetilde{h}_s}{\partial x_i} - \frac{\partial \overline{\rho}}{\partial t} - \widetilde{u}_j \frac{\partial \overline{\rho}}{\partial x_i} - \frac{\partial}{\partial x_i} \left(\lambda \frac{\partial \widetilde{T}}{\partial x_i} \right) = - \frac{\partial}{\partial x_j} \left[\overline{\rho} \left(\widetilde{u_i h_s} - \widetilde{u}_i \widetilde{h}_s \right) \right] \tag{6}$$

where h_s and λ are the sensible enthalpy and thermal conductivity, respectively.

The compressible subgrid enthalpy flux term is defined as [30,37]:

$$\overline{\rho} \left(\widetilde{u_i h_s} - \widetilde{u}_i \widetilde{h}_s \right) = - \frac{\mu_{SGS} C_P}{\mathrm{Pr}_{SGS}} \frac{\partial \widetilde{T}}{\partial x_i} \tag{7}$$

where μ_{SGS} denotes subgrid viscosity and Pr_{SGS} denotes the subgrid Prandtl number. In the present study, the wall−adapting local eddy−viscosity (WALE) model [30,37] was employed as the SGS model. The dynamic load−carrying capacity (DLCC), denoted as F_d, of the aerostatic bearing can be determined by integrating the pressure distribution on the wall surface. The dynamic load−carrying capacity can be defined as follows:

$$F_d = \int_0^R \int_0^{2\pi} (p_d - p_0) r dr d\theta \tag{8}$$

where p_d represents transient pressure.

The standard deviation of the DLCC can be defined as follows:

$$\sigma_f = \sqrt{\frac{\sum_{i=1}^{n} (F_{di} - F_m)}{n}} \tag{9}$$

where F_{di} represents the time−varying DLCC of the ith time step; F_m represents the LCC, which is the average value of DLCC; and n represents the number of iteration steps. The fluctuation force $F_f = F_{di} - F_m$ represents the fluctuation in the DLCC.

Stiffness can be expressed as follows:

$$K = \frac{dF_m}{dh} \tag{10}$$

3.2. Grid Generation and Boundary Conditions

The turbulent vortex structures in the aerostatic bearing with the PSOR were investigated in a quarter of the computational domain to optimize computational efficiency. Figure 4b illustrates the use of a hexahedral semi−refined unstructured grid to ensure the precision and reliability of the simulation results by using Altair's Hypermesh software. The Ansys CFD software Fluent was used for the simulations. Complex vortex structures in the chamber were investigated through the embedded large−eddy simulation (ELES) modeling technique. As illustrated in Figure 4a, a no−slip shear condition, no heat transfer conditions, and a perfectly smooth surface were applied as the boundary walls. Symmetrical boundaries were established on the two surfaces in the circumferential direction. Inlet pressure and outlet pressure were set at approximately 0.5 MPa and 0.1 MPa, respectively. The pressure−velocity coupling scheme employed the pressure−implicit with splitting of operators (PISO) algorithm [38]. To mitigate numerical dissipation, second−order upwind interpolation was applied to evaluate density, turbulent kinetic energy, and turbulent dissipation rate while employing bounded central differencing for momentum interpolation. Additionally, a second−order implicit scheme was used for transient simulation. The non−iterative time−advancement scheme [38] was employed to enhance numerical calculation efficiency and accuracy, with a time step size of $\Delta t = 1 \times 10^{-8}$ s, selected in accordance with the CFL condition $u\Delta t/\Delta x < 1$.Table 2 lists the physical constants of air, assumed to adhere to the ideal gas law.

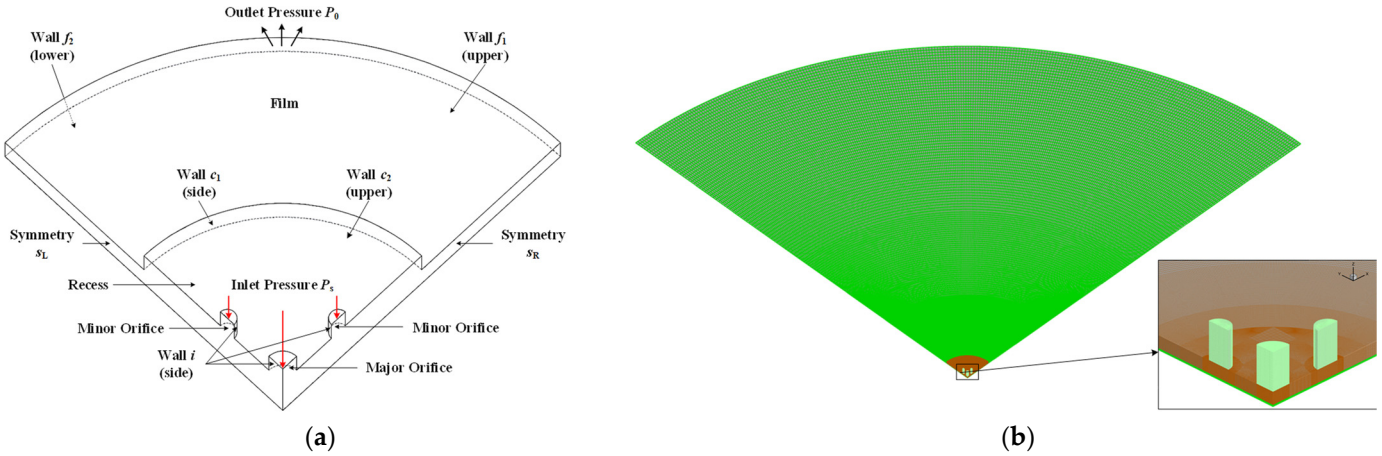

Figure 4. Type A aerostatic bearing: (**a**) computational domain and boundary conditions; (**b**) computational grids.

Table 2. Physical constants of the ideal air.

Air Temperature	Density	Specific Heat	Heat Conductivity	Viscosity	Molecular Weight
293.15 K	1.202 kg/m^3	1006.43 J/(kg·K)	0.0242 W/(m·K)	1.7894×10^{-5} kg/(m·s)	28.966×10^{-3} kg/mol

3.3. Mesh Grid Independent Analysis

Discrepancies attributable to the quantity and dimensions of grids can be mitigated based on the results of grid independence tests, which are considered complete when simulation results are no longer influenced by subsequent mesh refinement. The non−dimensional distance y^+, which characterizes the resolution scale of the grids near the wall and is maintained at a value lower than 1, can be mathematically represented as $y^+ = \sqrt{\rho \tau_w} y/\mu$) [30,34]. Here, τ_w represents the wall shear stress, and y denotes the length from the centroid of the initial layer grid near the wall region to its boundary. Table 3 presents the total numbers and volumes of grid elements within three distinct computational domains of the type A aerostatic bearing. However, the element count can be approximately equal only when the conditions remain constant despite the slight variations in the PSOR structures of aerostatic bearings. The mean force (F_m) and the standard deviation (σ_f) of the DLCC (F_d), as discussed in Section 4, are compared between the sparse−grid and refinement−grid cases, revealing that increasing the number of elements or implementing local grid refinement exerts minimal influence on the mean force or the standard deviation of the DLCC. The computational domain of aerostatic bearings with diverse PSOR configurations must be meshed with no fewer than two million elements to ensure both accuracy and computational efficiency.

Table 3. Grid independence analysis, where Δ denotes gird element volume (μm^3).

Type	Chamber		Orifice		Air Film		y^+_{max}	Total Number	Mean Force F_m/N	Standard Deviation σ_f
	Δ_{min}	Δ_{max}	Δ_{min}	Δ_{max}	Δ_{min}	Δ_{max}				
1	1.51	1714	21.66	81.27	894	6260	1.84	1,418,400	320.22	0.530
2	1.10	1203	21.66	81.27	1375	9630	1.51	2,181,621	324.72	0.525
3	0.55	469	21.66	81.27	1375	9630	0.65	3,278,216	325.16	0.527
4	0.03	281	21.66	81.27	1103	5643	0.46	4,134,320	325.06	0.522

4. Simulation Results and Discussion

4.1. Turbulent Vortex Formation Mechanism

To illustrate the complex mechanisms governing the formation and evolution of turbulent vortices within a multi−orifice restrictor, we provide a detailed depiction of airflow near the outlet of any two adjacent orifices in the aerostatic bearing's chamber, as depicted in Figure 5. As the high−speed, high−pressure airflow (A) exits through the orifice, it experiences a separation phenomenon when it encounters the top surface after the abrupt expansion of the airflow's cross−sectional area. An airflow channel (C) with a deflection angle (α) emerges between the compression zone (A) and the separation zone (B). When airflow (V_1) traverses the boundary layer between the separation zone (C) and the compression zone (B), an expansion wave (V_2) and a compression wave (V_3) are generated, respectively. Airflows (V_3 and V_4) progress towards the bottom surface through channel (C), and transform into airflow (V_5) because of the splash effect. Upon colliding with the top surface, the airflow (V_5) exhibits velocity separation, resulting in the formation of airflow (V_6) and airflow (V_7). Airflows originating from adjacent orifices exhibit opposing rotation directions and velocities, resulting in dynamic interactions that can generate intricate vortices. Different airflows with diverse flow directions and velocities engage in complex interactions with the surrounding air, leading to various turbulent vortices with distinct scales and intensities. Consequently, the interference of distinct airflows may induce complex and varying turbulent vortices. This continuous airflow initiates a perpetual cycle of vortex generation and dissipation, yielding a diverse array of turbulent vortices within the chamber.

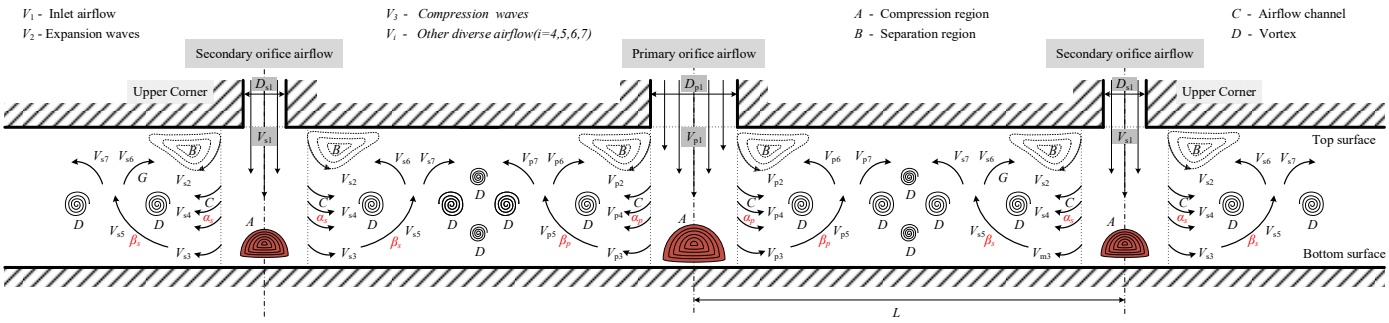

Figure 5. Mechanism of formation and evolution of turbulent vortices in a multi−orifice restrictor.

4.2. Transient Flow Behaviors

As illustrated in Figures 6 and 7, numerous turbulent vortices, characterized by distinctive sizes, shapes, and alternating rotational directions, are generated near the outlet of both primary and secondary orifices. The high−speed airflows from the primary and secondary orifices collide with the bottom surface and disperse in all directions. Moreover, a larger number of turbulent vortices are generated between the primary and secondary orifices because of the interplay of airflows from the primary and secondary orifices. Subsequently, turbulent vortices are generated and undergo sweeping and rolling up, eventually dissipating under the influence of viscosity. These turbulent vortices exhibit unsteady features, encompassing turbulent vortex generation, amplification, shedding, and eventual dissipation. Compared with the 2D flow field, the 3D flow dynamics of turbulent flow in the chamber facilitate a more comprehensive analysis of the variations in vortex structure and the mechanism of the nano−vibration suppression. Figure 8 depicts the time−varying fluctuation force of the DLCC. The evolution of turbulent vortices in the chamber engenders complex variations in pressure, resulting in nano−scale vibrations.

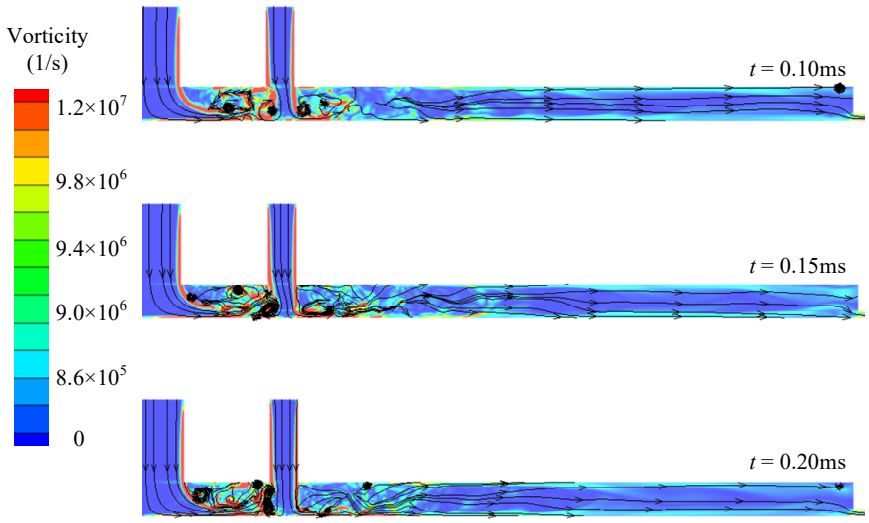

Figure 6. The 2D transient flow structures in the chamber of aerostatic thrust bearing with PSOR.

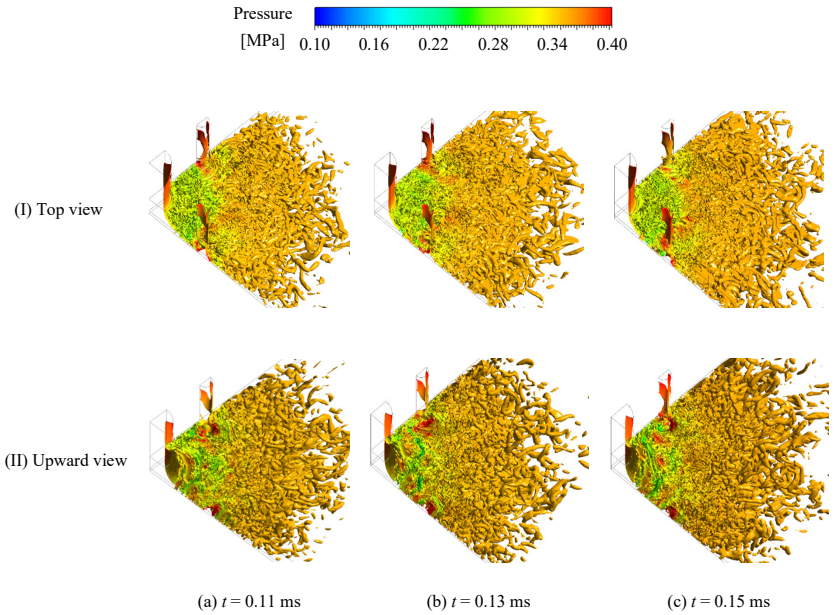

Figure 7. Iso−surfaces of instantaneous pressure about the vortex core region in chamber.

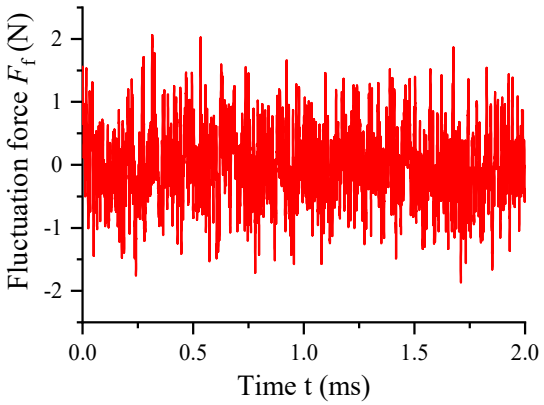

Figure 8. Time−varying fluctuation force of the DLCC of aerostatic thrust bearing with PSOR.

4.3. Effects of the Varying Diameter of Secondary Orifices on Nano−Vibration Characteristics

Simulations were conducted with constant structural parameters and operational conditions to determine the influence of varying secondary orifice diameters on the static and dynamic characteristics. The structural parameters (H_f = 25 μm), the boundary conditions (P_s = 0.5 Mpa and P_0 = 0.1 Mpa) and initial conditions for the aerostatic bearings are detailed in Tables 1 and 2.

Figure 9 illustrates the LCC, stiffness, and mass flow rate of aerostatic bearings concerning varying diameters of secondary orifices. With the increasing diameter of secondary orifices, the LCC of the aerostatic bearings increases, particularly in the presence of larger gas films. Concurrently, as the diameters of the secondary orifices increase, the stiffness decreases initially and then increases while the film thickness remains constant. Additionally, an increase in secondary orifice diameters is correlated with an increase in the mass flow rate. Consequently, the increase in secondary orifice diameters leads to an elevation in the LCC, while the stiffness decreases gradually.

Figure 10 illustrates the pressure distribution, vorticity, and velocity contours of the symmetry plane concerning various diameters of secondary orifices. Notably, as depicted in Figure 10a, with an increase in the diameter of secondary orifices, the pressure distribution in the chamber increases substantially and becomes uniform. Moreover, the amplitude of pressure fluctuations gradually decreases. As illustrated in Figure 10b, an increase in

the diameter of secondary orifices leads to increases in the vortex vorticity and complexity near the secondary orifice and between the primary orifice and the secondary orifices. Conversely, the changes in vortex vorticity and complexity distanced from the secondary orifice are negligible. Figure 10c indicates that the increase in the secondary orifice diameter reduce the velocity V_1 at both the primary and secondary orifices, accompanied by a gradual decrease in various velocities and velocity fluctuations in the chamber. Moreover, with the increase in the diameter of the secondary orifices, the stability of velocities in the chamber is enhanced. Unlike the aerostatic bearing with an SOR, the pressure distribution in the chamber of the bearing with a PSOR gradually increases with the increase in the diameter of the secondary orifice. Furthermore, compared with the bearing with SOR, the velocity, vortex vorticity intensity, and vortex intricacy for aerostatic bearings with smaller secondary orifice diameters increase because of the complex coupling effects between the primary orifice and secondary orifice. Conversely, these parameters are subdued relative to aerostatic bearings with larger secondary orifice diameters because of the influence of volume ratio. According to the aforementioned analysis, the increase in the diameter of the secondary orifices involves an increase in the total area and mass flow rate of these orifices. Consequently, the distribution of pressure is enhanced, and the velocities at the primary orifice and the secondary orifices decrease. Additionally, the effects of turbulent velocities and the interaction between the primary orifice and secondary orifices are mitigated. Subsequently, increasing the diameter of the secondary orifices inhibits vortex generation and reduces pressure fluctuations.

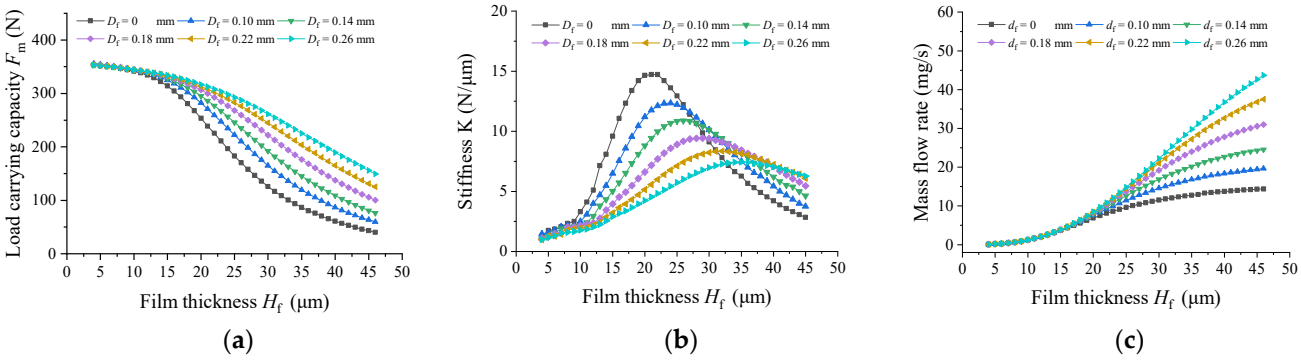

Figure 9. (**a**) LCC; (**b**) stiffness; (**c**) mass flow rate.

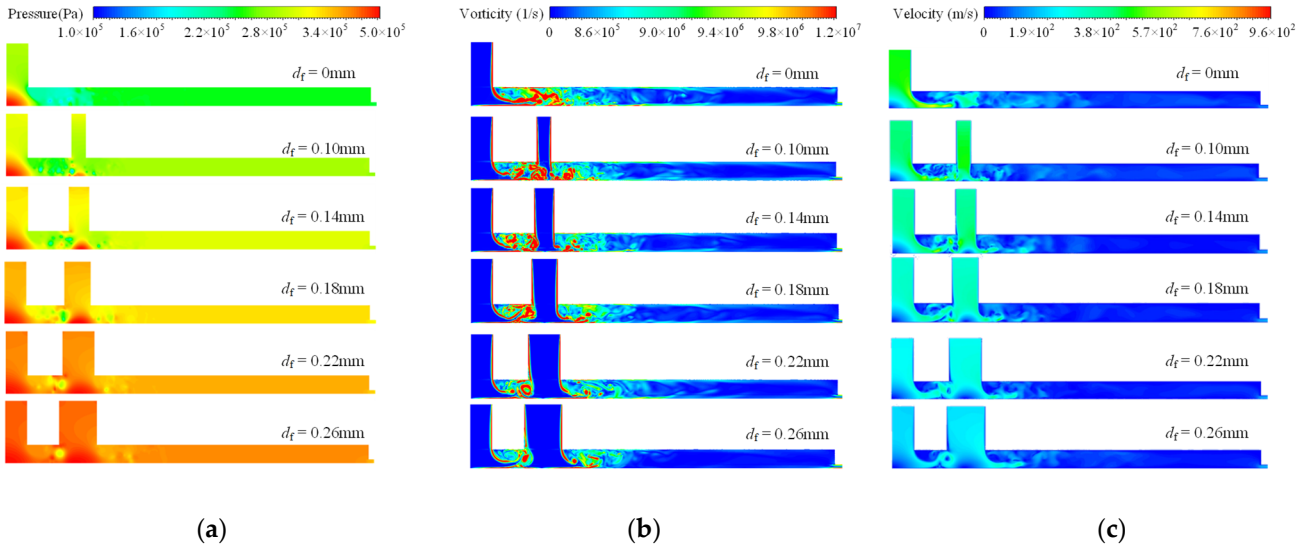

Figure 10. (**a**) Pressure distribution; (**b**) vorticity; (**c**) velocity contours.

Figure 11 depicts the 3D iso−surfaces of vorticity in the chamber, demonstrating the influence of varying secondary orifice diameters. With an increase in the diameter of the secondary orifice, the region characterized by turbulent vortices expands gradually. Simultaneously, the vorticity magnitude of turbulent vortices decreases gradually. Furthermore, an increase in the diameter of the secondary orifices enhances the stability and orderliness of the turbulent vortex structures both at the periphery of the secondary orifice and between the primary orifice and the secondary orifices. In comparison with aerostatic bearing with a SOR, as the secondary orifice diameter increases, the area of the turbulent vortex core region first decreases and then increases, while the turbulent intensity first increases and then decreases. Consequently, the augmentation of the secondary orifice diameter effectively inhibits the vortex generation and mitigates the pressure fluctuations.

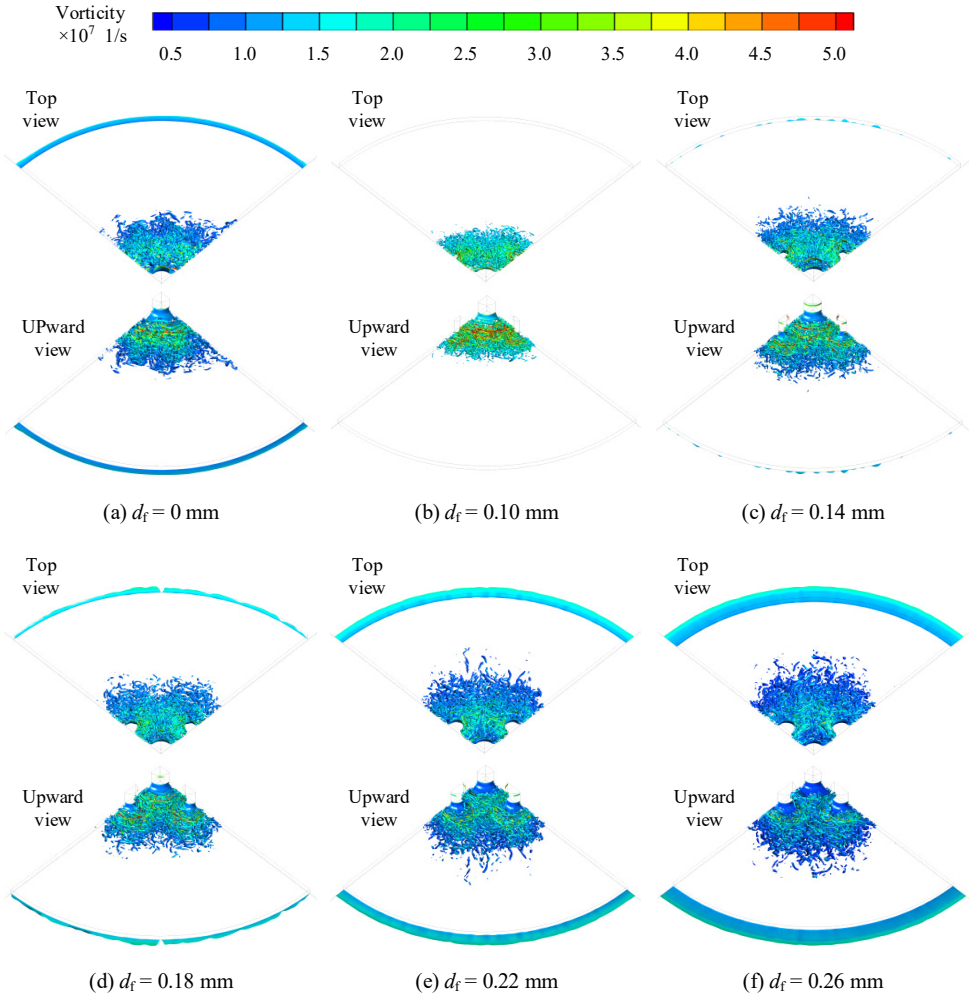

Figure 11. Iso−surfaces of vorticity in the chamber.

Figure 12 illustrates the time−varying fluctuation force (F_f) and its corresponding standard deviation (σ_f) of the DLCC of aerostatic bearings with varying secondary orifice diameters. An increase in the diameter of the secondary orifices leads to a reduction in both the fluctuation force (F_f) and the standard deviation (σ_f) of the DLCC. The computed results of the fluctuation force are highly consistent with the results obtained through the analyses of turbulent vortices. Thus, noticeable decrease in the secondary orifice diameter yields a discernible reduction in nano−vibrations and an enhancement in system stability.

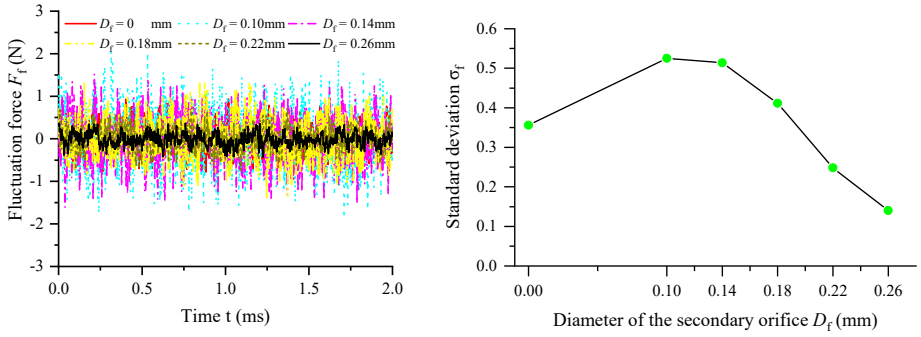

Figure 12. The DLCC of aerostatic bearings with varying diameters of secondary orifices: (**a**) time−varying fluctuation force; (**b**) standard deviation of DLCC.

5. Experiment Results

Two experimental configurations were constructed to validate the accuracy of the numerical models and elucidate the underlying suppression mechanism of the PSORs. These setups aimed to measure the LCC and nano−vibration of aerostatic bearings with varying PSORs.

5.1. Tested Aerostatic Bearings

As depicted in Figure 13, the experimental aerostatic bearing comprised two components: the aerostatic bearing pad and the primary and secondary orifice restrictor, both fabricated using cylindrical aluminum alloy. The orifice restrictor, integrated into the chamber of the aerostatic bearing pad, features secondary orifices with varying diameters. Precision techniques such as pico−second laser drilling and ultrasonic technology were employed to manufacture the PSOR, ensuring high quality, uniformity, and small orifice sizes. Figure 13b displays electron microscopy images of the orifice restrictors, showcasing aerostatic bearings with secondary orifice diameters of D_s = 0.1 mm and D_s = 0.26 mm. Furthermore, a SOR is composed of a cylindrical ruby. The structural parameters of three aerostatic bearings with a diameter of 80 mm are listed in Table 4.

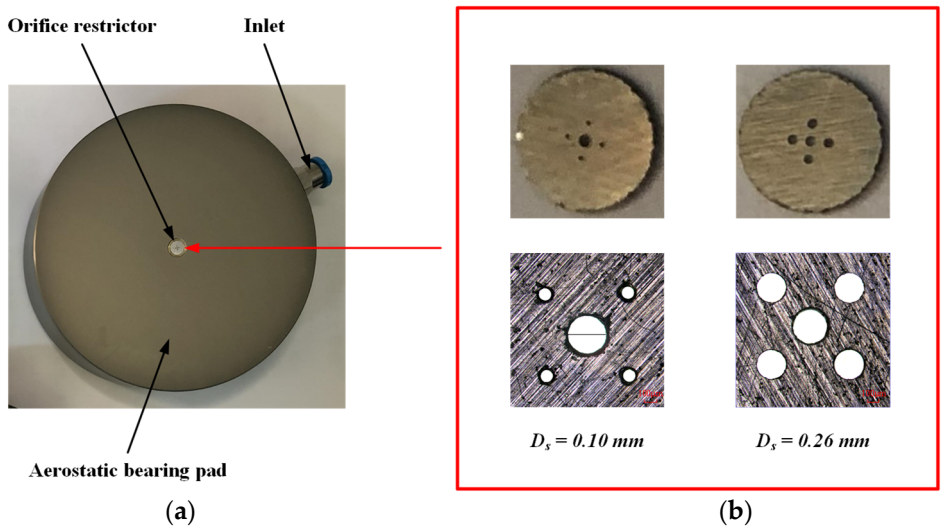

Figure 13. (**a**) Photograph of type A aerostatic thrust bearing; (**b**) shape inspection of PSOR by electron microscope.

Table 4. Structural parameters of aerostatic bearings.

Type	Restrictor	Primary Orifice Diameter D_p (mm)	Secondary Orifice Diameter D_s (mm)	Spacing L (mm)	Chamber Height H_c (mm)	Chamber Diameter D_c (mm)	Orifice Height H_r (mm)
A1	1 Po + 4 So	0.3	0.10	0.5	0.1	5	0.3
A2	1 Po + 4 So	0.3	0.26	0.5	0.1	5	0.3
B	1 Po	0.3	0	0	0.1	5	0.3

5.2. Load−Carrying Capacity Testing and Analyzing

An experimental platform was constructed for evaluating the static performance, as illustrated in Figure 14. This setup primarily consists of a marble platform, the three tested aerostatic bearings (Type A_1, Type A_2, and Type B), a proportional throttle valve, a resistance strain force sensor (PBCL, ranging from 200 Kg to 700 Kg; Zhongjing, Shanghai, China), an air cylinder, and an inductance micrometer (TESA® TT20−GTL22 with a 0.1 µm resolution, range ±2 mm; Lausanne Switzerland). The film thickness was recorded by the inductance micrometer affixed to the marble and adjusted by altering the cylinder pressure through the proportional throttle valve. The LCC was measured by the resistance strain force sensor. The mean value was determined through numerous measurements.

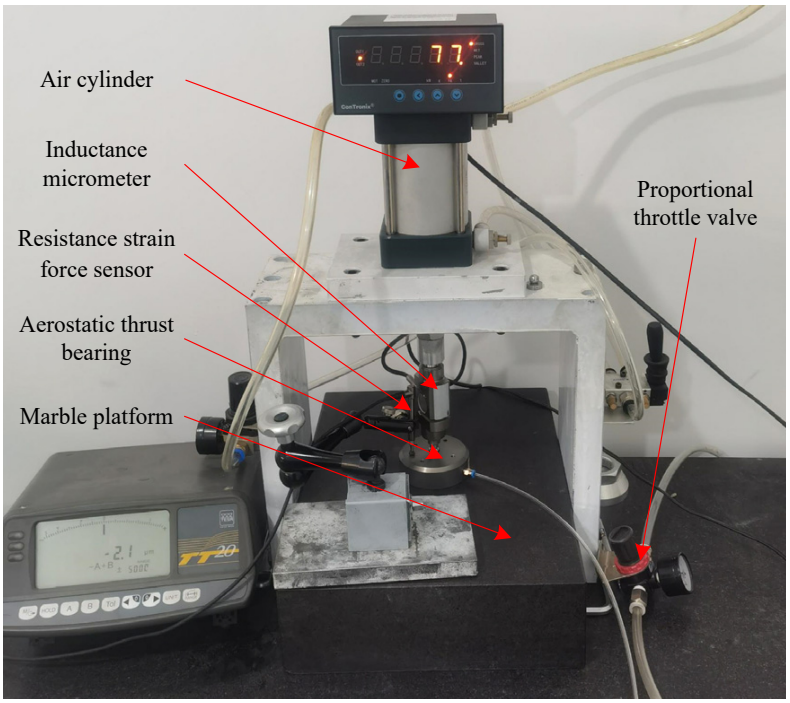

Figure 14. Static performance experimental platform.

The LCC F_m of the three aerostatic bearings is plotted in Figure 15 and can be expressed as a function of film thickness, ranging from 5 to 30 µm, while the supply air pressure is P_s = 0.5 MPa. Notably, the calculation results are highly consistent with the experimental results for all three aerostatic bearings. Notably, their LCC gradually increases with the increase in the diameter of the secondary orifices, especially when the film thickness is relatively large. The results indicated that the enhancement of the secondary orifice diameter effectively increases their LCC, validating the reasonableness of the LES simulation.

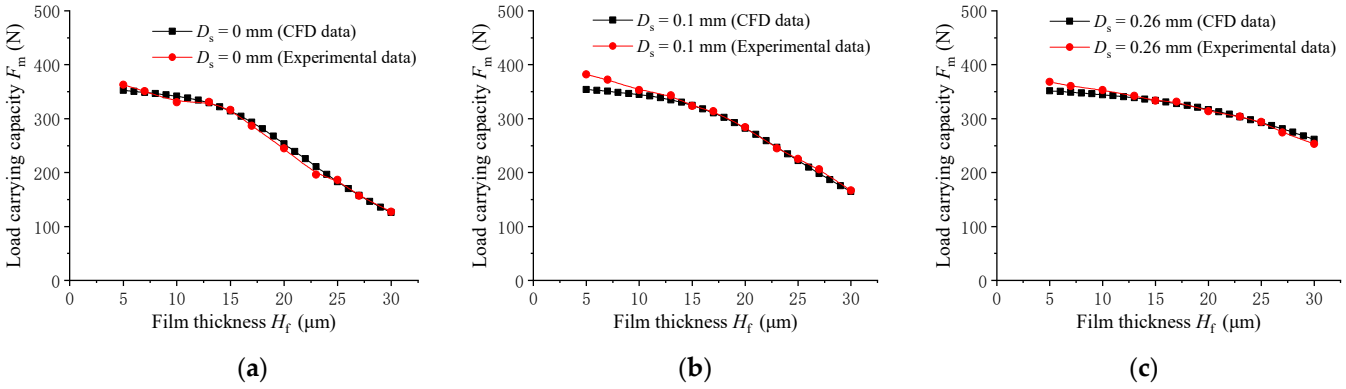

Figure 15. Comparing the experimental and numerical results: (**a**)Type *B*; (**b**) Type A_1; (**c**) Type A_2.

5.3. Nano−Vibration Testing and Analyzing

An experimental platform was constructed for measuring nano−vibrations, as shown in Figure 16. The setup consisted of three aerostatic bearings (Type A_1, Type A_2, and Type *B*), different weights, an acceleration sensor (Lancetec−ULT−2015 with 0.000004 g resolution; QUATR, Beijing, China), a laser displacement sensor (LK−G155H with a 0.5 μm resolution; KEYENCE, Osaka, Japan), a marble platform (with roughness < 1 μm), an optical platform, a data acquisition card (NI−9234, 24−bit; Texas, USA), and a personal computer terminal (Lenovo, Beijing, China) with data analysis software (LMS Test Lab, LMS, Texas, USA). The aerostatic bearings were placed on the marble table. The acceleration sensor was installed on the weights. The film thickness was recorded by the laser displacement sensor affixed to the marble and adjusted by varying the weights. The tested nano−vibration data were acquired by the acceleration sensor and processed on the PC terminal using data analysis software. Moreover, all the experiments were conducted on an optical bench with a natural frequency of only 1.5–5 Hz to minimize vibration disturbance from the external environment.

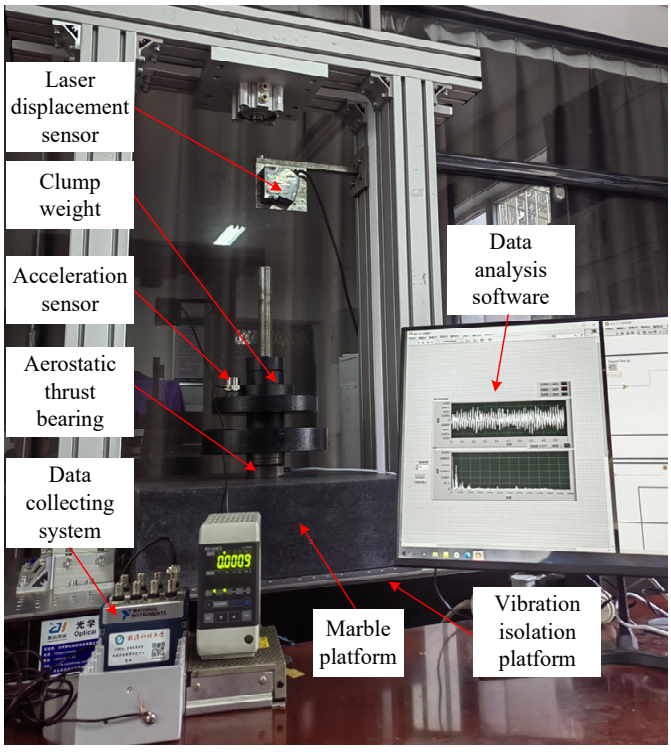

Figure 16. Photo of experiment platform for vibration.

Figure 17 illustrates the experimental acceleration data acquired for three aerostatic bearings in both the time and frequency domains, with a supply pressure of P_s = 0.5 MPa and a film thickness of H_f = 25 μm. Frequency−domain data were acquired through the fast Fourier transform operations on time−domain signals. The dominant frequency peak is primarily concentrated below 1000 Hz. Notably, among these three types of aerostatic bearings, Type A_2 exhibited the weakest acceleration amplitude, while Type A_2 exhibited the highest acceleration magnitude. Hence, the magnitudes of both the time and frequency domains of the Type B aerostatic bearing exceed those of the Type A_2 aerostatic bearing but are lower than the magnitudes of the Type A_1 aerostatic bearing. Aerostatic bearings with smaller secondary orifice diameters exacerbate nano−vibrations, whereas those with larger secondary orifice diameters mitigate nano−vibrations, confirming the rationality and effectiveness of the model. The results indicated that the rational optimization design of the PSOR can effectively suppress nano−vibrations in aerostatic bearings, enhancing their stability.

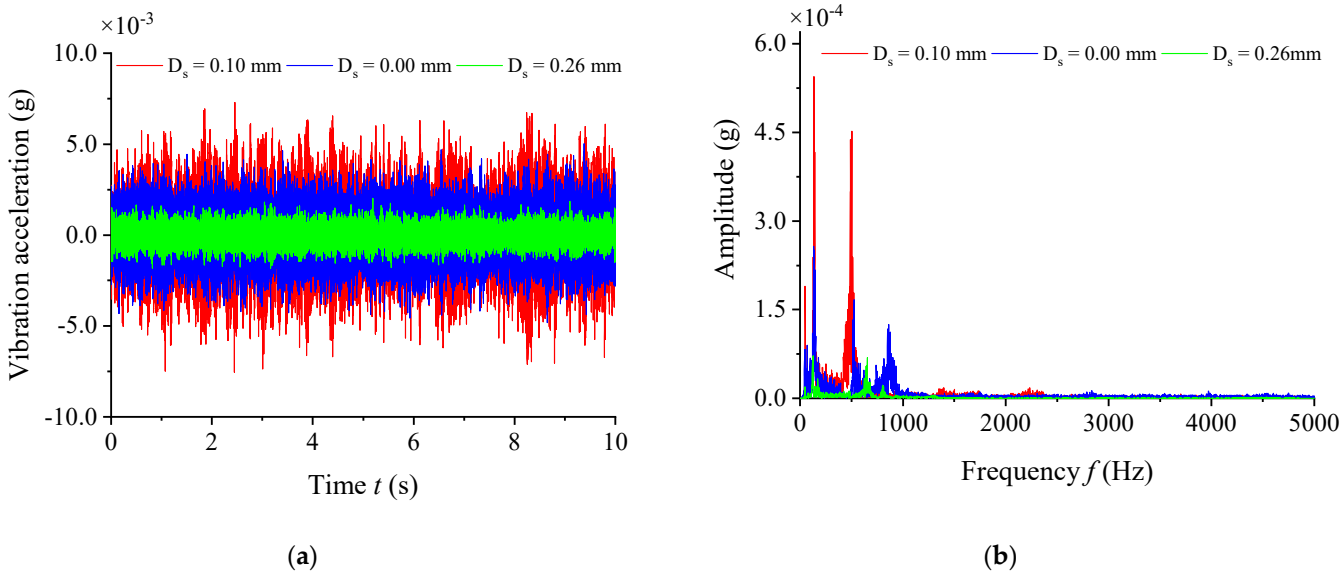

Figure 17. (**a**) Acceleration signal in the time domain for three aerostatic bearings; (**b**) acceleration signal in the frequency domain for three aerostatic bearings.

6. Conclusions

This paper introduces a novel aerostatic bearing with a PSOR designed to enhance the LCC, suppress turbulent vortex generation, and alleviate nano−vibrations. The effects of varying secondary orifice diameters on their static and dynamic performance were investigated through numerical simulation and experimentation. The LES method was employed to study the transient flow characteristics of aerostatic bearings with both the SOR and the PSOR to resolve the complex turbulent vortex structure. In addition, the formation mechanism of turbulent vortex and interaction dynamics among the primary orifice and secondary orifices were investigated. The experimental results indicated a high level of consistency with the numerical results, confirming the accuracy of the simulation model and the effectiveness of the PSOR. Increasing the diameter of the secondary orifice can improve the pressure distribution, reduce velocity, and suppress the turbulent vortex formation in the chamber, thereby enhancing the LCC and mitigating pressure fluctuations. Among the five proposed aerostatic bearings, the one with a secondary orifice diameter of 0.1 mm demonstrated the smallest LCC and largest turbulent vortices in the chamber, followed by those with diameters of 0.14 mm, 0.18 mm, and 0.22 mm, respectively. Consequently, the aerostatic bearing with a 0.26 mm secondary orifice, with the largest LCC and the smallest turbulent vortices, demonstrated the most stable structure. Therefore, while increasing the diameter of the secondary orifice enhances the LCC and reduces vibrations, the diameters of

excessively large secondary orifices must be selected with caution because of the potential occurrence of the hammer phenomenon.

This study may serve as a valuable point of reference for further understanding and mitigating the nano−vibrations in aerostatic bearings. It provides insights into the formation mechanism of turbulent vortices and the interaction dynamics among the primary orifice and secondary orifices. Future studies may investigate internal airflow field characteristics in aerostatic bearings within the recess using techniques such as particle image velocimetry (PIV).

Author Contributions: Conceptualization, P.Y. and L.Z.; methodology, P.Y. and L.Z.; software, T.Z. and J.L.; validation, P.Y. and T.Z.; writing—review and editing, P.Y. and L.Z.; investigation, M.Z.; resources, P.Y. All authors have read and agreed to the published version of the manuscript.

Funding: This research was funded by the National Natural Science Foundation of China, grant number 51705378; and the Regional Joint Foundation of the National Natural Science Foundation of China, grant number U21A2057.

Data Availability Statement: Data are contained within the article.

Acknowledgments: Numerical calculation is supported by the High−Performance Computing Center of Wuhan University of Science and Technology. The authors would like to thank all the reviewers who participated in the review of this manuscript.

Conflicts of Interest: The authors declare no conflict of interest.

Nomenclature

D	aerostatic bearing outer diameter	V_i	airflows velocity (i = 1, 2, 3, 4, 5, 6, 7)
D_p	primary orifice diameter	τ_w	wall shear stress
D_s	secondary orifice diameter	Δ	gird element volume
D_c	chamber diameter	σ_{ij}	viscous stress tensor
H_c	height of compression area	τ_{ij}	subgrid−scale (SGS) stress
H_r	restrictor height	m	mass flow rate
H_f	air film thickness	t	time
P_s	air supply pressure	x_i, x_j, x_k	coordinates in various directions
P_0	atmosphere pressure	u_i, u_j, u_k	flow velocities in various directions
H_c	cylindrical chamber height	R_e	Reynolds number
K	stiffness	T	temperature
L	spacing between the primary orifice and the secondary orifice	μ	air viscosity
ρ	air density	Δx	size of the control volume
p	dynamic pressure	R	ideal gas constant
α	angle of the flow V_3	Δt	time step size
β	angle of the flow V_4	p_d	dynamic pressure
R_{ij}	SGS Reynolds stresses	F_d	dynamic load−carrying capacity (DLCC)
C_{ij}	cross stresses	F_m	mean force
L_{ij}	subgrid−scale Leonard stresses	F_f	fluctuation force of the DLCC
δ_{ij}	Kronecker delta function	σ_f	standard deviation of the DLCC

References

1. Lian, H.; Rong, C.; Li, Y. Influence of Operating Temperature on the Static Characteristics of an Externally Pressurized Thrust Bearing Lubricated with Refrigerant Gas. *Tribol. Lett.* **2021**, *69*, 123. [CrossRef]
2. Ise, T.; Arita, N.; Asami, T.; Kawashima, I.; Maeda, T.; Nakajima, T. Experimental study of small−size air turbo blower supported by externally pressurized conical gas bearings. *Mech. Mach. Theory* **2015**, *84*, 57–66. [CrossRef]
3. Lu, Z.W.; Zhang, J.A.; Liu, B. Study on the Gas Film Flow Field and its Influencing Factors at the Outlet of the Orifice of the Aerostatic Bearing. *Shock Vib.* **2020**, *2020*, 8891382. [CrossRef]
4. Chang, S.H.; Chan, C.W.; Jeng, Y.R. Numerical analysis of discharge coefficients in aerostatic bearings with orifice−type restrictors. *Tribol. Int.* **2015**, *90*, 157–163. [CrossRef]

5. Majumdar, B.C. Zero−load stability of a rigid rotor supported on pressurized porous gas bearings. *Mech. Mach. Theory* **1977**, *12*, 303–310. [CrossRef]
6. Lohiya, S.H.; Pande, S.S. Analysis of tapered land aerostatic thrust bearing operating under nonsteady loads. *Mech. Mach. Theory* **1989**, *24*, 515–521. [CrossRef]
7. Chen, M.F.; Lin, Y.T. Static behavior and dynamic stability analysis of grooved rectangular aerostatic thrust bearings by modified resistance network method. *Tribol. Int.* **2002**, *35*, 329–338. [CrossRef]
8. Sahto, M.P.; Wang, W.; Imran, M.; He, L.; Li, H.; Weiwei, G. Modelling and Simulation of Aerostatic Thrust Bearings. *IEEE Access* **2020**, *8*, 121299–121310. [CrossRef]
9. Colombo, F.; Lentini, L.; Raparelli, T.; Trivella, A.; Viktorov, V. Dynamic characterisation of rectangular aerostatic pads with multiple inherent orifices. *Tribol. Lett.* **2018**, *66*, 133. [CrossRef]
10. Belforte, G.; Raparelli, T.; Trivella, A.; Viktorov, V.; Visconte, C. CFD analysis of a simple orifice−type feeding system for aerostatic bearings. *Tribol. Lett.* **2015**, *58*, 25. [CrossRef]
11. Kassab, S.Z. Empirical correlations for the pressure depression in externally pressurized gas bearings. *Tribol. Int.* **1997**, *30*, 59–67. [CrossRef]
12. Kassab, S.Z.; Noureldeen, E.M.; Shawky, M.A. Effects of operating conditions and supply hole diameter on the performance of a rectangular aerostatic bearing. *Tribol. Int.* **1997**, *30*, 533–545. [CrossRef]
13. Nishio, U.; Somaya, K.; Yoshimoto, S. Numerical calculation and experimental verification of static and dynamic characteristics of aerostatic thrust bearings with small feedholes. *Tribol. Int.* **2011**, *44*, 1790–1795. [CrossRef]
14. Boffey, D.A.; Duncan, A.E.; Dearden, J.K. An experimental investigation of the effect of orifice restrictor size on the stiffness of an industrial air lubricated thrust bearing. *Tribol. Int.* **1981**, *14*, 287–291. [CrossRef]
15. Boffey, D.; Barrow, A.A.; Dearden, J.K. Experimental investigation into the performance of an aerostatic industrial thrust bearing. *Tribol. Int.* **1985**, *18*, 165–168. [CrossRef]
16. Chen, Y.S.; Chiu, C.C.; Cheng, Y.D. Influences of operational conditions and geometric parameters on the stiffness of aerostatic journal bearings. *Precis. Eng.* **2010**, *34*, 722–734. [CrossRef]
17. Chen, X.D.; He, X.M. The effect of the recess shape on performance analysis of the gas−lubricated bearing in optical lithography. *Tribol. Int.* **2006**, *39*, 1336–1341. [CrossRef]
18. Li, Y.; Han, D. Influences of the geometrical parameters of aerostatic thrust bearing with pocketed orifice −type restrictor on its performance. *Tribol. Int.* **2007**, *40*, 1120–1126. [CrossRef]
19. Salem, E.; Kamal, W. Effect of recess geometry on shock wave formation in circular gas bearings. *Wear* **1978**, *46*, 351–366. [CrossRef]
20. Talukder, H.M.; Stowell, T.B. Pneumatic hammer in an externally pressurized orifice−compensated air journal bearing. *Tribol. Int.* **2003**, *36*, 585–591. [CrossRef]
21. Fourka, M.; Tian, Y.; Bonis, M. Prediction of the stability of air thrust bearings by numerical, analytical and experimental methods. *Wear* **1996**, *198*, 1–6. [CrossRef]
22. Kawai, T.; Ebihara, K.; Takeuchi, Y. Improvement of machining accuracy of 5−axis control ultraprecision machining by means of laminarization and mirror surface finishing. *CIRP Ann.* **2005**, *54*, 329–332. [CrossRef]
23. Yoshimura, T.; Hanafusa, T.; Kitagawa, T.; Hirayama, T.; Matsuoka, T.; Yabe, H. Clarifications of the mechanism of nano−fluctuation of aerostatic thrust bearing with surface restriction. *Tribol. Int.* **2012**, *48*, 29–34. [CrossRef]
24. Chen, X.; Han, C.; Xin, L.; Ye, Y.; Hu, Y.; Xu, J. Air Vortices and Nano−Vibration of Aerostatic Bearings. *Tribol. Lett.* **2011**, *42*, 179–183. [CrossRef]
25. Eleshaky, M.E. CFD investigation of pressure depressions in aerostatic circular thrust bearings. *Tribol. Int.* **2009**, *42*, 1108–1117. [CrossRef]
26. Otsu, Y.; Somaya, K.; Yoshimoto, S. High−speed stability of a rigid rotor supported by aerostatic journal bearings with compound restrictors. *Tribol. Int.* **2011**, *44*, 9–17. [CrossRef]
27. Wang, P.; Zhang, Y.; Feng, L.; Hou, W.; Wang, J.; Li, W.; Feng, K. Study on the pneumatic hammer phenomenon of aerostatic bearings based on the empirical mode method: Numerical and experimental analysis. *Tribol. Int.* **2023**, *181*, 108305. [CrossRef]
28. Aoyama, T.; Kakinuma, Y.; Kobayashi, Y. Numerical and Experimental Analysis for the Small Vibration of Aerostatic Guideways. *CIRP Ann.—Manuf. Technol.* **2006**, *55*, 419–422. [CrossRef]
29. Ma, W.; Cui, J.; Liu, Y.; Tan, J. Improving the pneumatic hammer stability of aerostatic thrust bearing with recess using damping orifices. *Tribol. Int.* **2016**, *103*, 281–288. [CrossRef]
30. Zhu, J.; Chen, H.; Chen, X. Large eddy simulation of vortex shedding and pressure fluctuation in aerostatic bearings. *J. Fluids Struct.* **2013**, *40*, 42–51. [CrossRef]
31. Yifei, L.; Yihui, Y.; Hong, Y.; Xinen, L.; Jun, M.; Hailong, C. Modeling for optimization of circular flat pad aerostatic bearing with a single central orifice−type restrictor based on CFD simulation. *Tribol. Int.* **2017**, *109*, 206–216. [CrossRef]
32. Chen, X.; Chen, H.; Zhu, J.; Jiang, W. Vortex suppression and nano−vibration reduction of aerostatic bearings by arrayed microhole restrictors. *J. Vib. Control* **2017**, *23*, 842–852. [CrossRef]
33. Feng, K.; Wang, P.; Zhang, Y.; Hou, W.; Cui, H. Novel 3−D printed aerostatic bearings for the improvement of stability: Theoretical predictions and experimental measurements. *Tribol. Int.* **2021**, *163*, 107149. [CrossRef]

34. Yu, P.; Lu, J.; Luo, Q.; Li, G.; Yin, X. Optimization Design of Aerostatic Bearings with Square Micro−Hole Arrayed Restrictor for the Improvement of Stability: Theoretical Predictions and Experimental Measurements. *Lubricants* **2022**, *10*, 295. [CrossRef]
35. Li, L.; Lou, J.; Nishikawa, H.; Luo, H. Reconstructed Discontinuous Galerkin Methods for Compressible Flows Based on a New Hyperbolic Navier−Stokes system. *J. Comput. Phys.* **2020**, *427*, 110058. [CrossRef]
36. Li, Y.; Zhao, J.; Zhu, H.; Lin, Y. Numerical analysis and experimental study on the microvibration of an aerostatic thrust bearing with a pocketed orifice−type restrictor. *ARCHIVE Proc. Inst. Mech. Eng. Part J J. Eng. Tribol. 1994−1996 (Vols 208–210)* **2014**, *229*, 609–623. [CrossRef]
37. Nicoud, F.; Ducros, F. Subgrid−Scale Stress Modelling Based on the Square of the Velocity Gradient Tensor. *Flow Turbul. Combust.* **1999**, *62*, 183–200. [CrossRef]
38. Issa, R.I. Solution of the implicitly discretised fluid flow equations by operator−splitting. *J. Comput. Phys.* **1991**, *62*, 40–65. [CrossRef]